



ELSEVIER

Ultramicroscopy 62 (1996) 103–121

ultramicroscopy

Structure projection retrieval by image processing of HREM images taken under non-optimum defocus conditions

Xiaodong Zou ^{a,*}, Margareta Sundberg ^b, Maxim Larine ^c, Sven Hovmöller ^a^a Structural Chemistry, Stockholm University, S-106 91 Stockholm, Sweden^b Inorganic Chemistry, Stockholm University, S-106 91 Stockholm, Sweden^c SoftHard Technology Ltd, Tvarožkova 8, 811 03 Bratislava, Slovakia

Received 13 December 1994; accepted 25 August 1995

Abstract

A direct method for retrieval of the projected potential from a single HREM image of a thin sample is presented. Both out-of-focus and astigmatic images can be restored. The defocus and astigmatism values are first determined from the Fourier transform of the digitised HREM image. Then a filter is applied which reverts the phases of those Fourier components which have been reversed by the Contrast Transfer Function (CTF). The method has been incorporated into the CRISP image processing system. It can be applied on any sample, crystalline or amorphous. From thin crystalline areas the projected symmetry can be determined and a further improvement achieved by imposing the symmetry exactly. This compensates for the effects of crystal tilt. Five HREM images of a thin crystal of $K_{8-x}Nb_{16-x}W_{12+x}O_{80}$ ($x \approx 1$), taken with different defocus and astigmatism values, were processed. Only one, taken near Scherzer defocus, was directly interpretable before image processing. After processing, all images showed the projected potential of the structure. Using data to 2.77 Å resolution, all heavy (Nb/W) atom positions were found in every image, within on average 0.15 Å of the positions determined by single crystal X-ray diffraction. In the HREM images taken under non-optimum defocus conditions, also the potassium atoms in the tunnels of the structure were found.

1. Introduction

Modern electron microscopes are capable of giving images with atomic resolution, i.e. with details as fine as the closest interatomic distances, which for all chemical compounds are in the range 1.2–2.5 Å (disregarding hydrogens). Unfortunately, high resolution electron microscopy (HREM) images are not always directly interpretable in terms of (projected) structure. There are a number of reasons for this, stemming both from the specimen under observation

and the electron optics. A large body of theoretical treatments of the scattering and image formation processes have been published, as well as several schemes for the reconstruction of projected structure from experimental HREM images.

The main advantage with electrons over X-rays or neutrons for studying atomic structure is of course that electrons can be focused into an image. For crystals this means that not only amplitudes, but also phases of the structure factors can be measured experimentally. However, the phases and amplitudes change with defocus. The phases outside the first zero crossover of the CTF are reversed, relative to

* Corresponding author.

those inside the crossover. The CTF changes rapidly with defocus, and as a result HREM images can have reversed contrast after changing the defocus a few hundred ångström. In order to explain this effect and the effects of sample thickness and aid in interpreting HREM images, image simulation programs were developed, first by O'Keefe [1], later to become the SHRLI set of programs. Image simulations soon became a standard tool for interpreting HREM images. Since both defocus and sample thickness usually are unknown, typically a matrix of some 5×5 images are simulated and compared with the experimental image or through-focus series of images. Usually crystal tilt and astigmatism are not considered when images are simulated, perhaps mainly because that would soon demand hundreds of images to be simulated.

However, the defocus and astigmatism need not be considered as unknown variables. Thon showed already in 1966 [2] that the CTF can be determined experimentally from an optical diffraction pattern of an image. In 1971 Erickson and Klug [3] showed how the defocus could be measured and compensated for qualitatively by optical diffraction and even quantitatively by computer-generated Fourier transforms. This soon became a standard tool in high-resolution imaging of biological samples. Erickson and Klug suggested that the true object transform could be obtained by dividing the image (Fourier) transform by $\sin \chi(\mathbf{u})$ of the CTF. They also commented that this process would lead to a division by zero near the zero crossovers of the CTF, so the information near these crossovers is lost. "These may be only a small part of the whole transform and may be negligible for the reconstruction of the compensated image. If not, they would have to be determined from other micrographs at slightly different values of defocusing where the zeros of $\sin \chi(\mathbf{u})$ occur at different values of \mathbf{u} . A system like this has been proposed and outlined by Schiske (1968) [4]".

The method by Erickson and Klug [3] was intended for negatively stained protein samples, where the resolution of the sample is typically limited to about 20 Å. It was soon extended to 7 Å resolution by Unwin and Henderson [5] who introduced low-dose imaging of unstained protein crystals. Further improvements, including refinement of defocus and astigmatism values to within 5 Å accuracy, by com-

paring amplitudes in individual images to very accurate electron diffraction amplitudes, led to a resolution of 3.5 Å for the protein bacteriorhodopsin [6].

In the meantime a "focus variation method" has been developed as a BRITE/EURAM project "to retrieve the structural information of the object directly from the experimental electron micrographs" especially for inorganic samples [7]. The first experimental results were obtained from an equidistant series of twenty 512×512 images, acquired using a slow-scan CCD camera on a field emission gun microscope. In a recent paper [8] Saxton claims that the focus variation method is essentially the same as that proposed earlier by Schiske [4].

In the present investigation we show that it is indeed possible to retrieve the projected structure from any single HREM image of a strongly scattering metal oxide, using the methods originally developed for proteins. Defocus and astigmatism are quantitatively estimated from the Fourier transform of the image and the phases corrected accordingly. Every single image out of five with very different defocus and astigmatism gave the correct structure. Atomic coordinates were measured and found to be within 0.15 Å of the values obtained by single crystal X-ray diffraction. The combination of data from several images, taken at different defocus to fill in the gaps near the CTF crossovers, was easily done, but did not result in any dramatic increase in image quality.

The procedure is now available as a tool inside the CRISP system for image processing of electron micrographs [9]. It can be used both for crystalline and non-crystalline objects, but the best results are obtained for crystals, partly because the crystal tilt can then be eliminated by imposing the (projected) crystal symmetry, as determined by the program.

2. Methods

2.1. Image formation and the contrast transfer function

Imaging by electrons can be divided into two main steps: (1) electrons interact with matter and (2) images are formed by the lens system.

(1) When electrons pass through a thin, weakly scattering object (weak-phase-object approximation

(WPO)), an incident electron wave with wavelength λ and amplitude 1 will be transmitted to a wave function:

$$\psi(\mathbf{r}) = \exp[-i\sigma\varphi(\mathbf{r})] \approx 1 - i\sigma\varphi(\mathbf{r}), \quad (1)$$

where $\varphi(\mathbf{r})$ is the projected potential distribution, $\sigma = 2\pi me\lambda/h^2$ is the interaction constant, h is Planck's constant, and e and m are electron charge and mass.

(2) When electrons pass through an objective lens, electron waves propagating along different directions are transferred differently. The function $T(\mathbf{u})$ which expresses how electron waves are transferred is called the contrast transfer function (CTF) and can be expressed as follows:

$$T(\mathbf{u}) = \mathcal{F}[t(\mathbf{r})] = A(\mathbf{u}) \sin \chi(\mathbf{u}), \quad (2)$$

$$A(\mathbf{u}) = \exp\left[-\pi^2\Delta^2\lambda^2\mathbf{u}^4/2\right] \times \exp\left[-\pi^2\alpha^2\mathbf{u}^2(\epsilon + C_s\lambda^2\mathbf{u}^2)^2\right], \quad (3)$$

$$\chi(\mathbf{u}) = \pi\epsilon\lambda\mathbf{u}^2 + \frac{1}{2}\pi C_s\lambda^3\mathbf{u}^4, \quad (4)$$

where $t(\mathbf{r})$ is the corresponding contrast transfer function in real space, \mathcal{F} is the Fourier transform operator, $\sin \chi(\mathbf{u})$ is a function of the defocus value ϵ , the spherical aberration constant C_s and the electron wavelength λ . $A(\mathbf{u})$ is the envelop function of the CTF, Δ the focus spread, α the electron beam divergence and \mathbf{r} , \mathbf{u} are vectors in real and reciprocal space, respectively [10]. Among those parameters which affect $T(\mathbf{u})$, the defocus value is the main parameter to be determined, since it is changed from image to image, while the other parameters are either instrument constants such as C_s or vary only little from one exposure to the next, as is the case with Δ and α .

When the electron waves are focused into an image, HREM images are formed. If the second order terms are neglected, the intensity distribution in the images becomes

$$I(\mathbf{r}) = |\psi(\mathbf{r}) * t(\mathbf{r})|^2 \approx 1 + 2\sigma\varphi(\mathbf{r}) * \mathcal{F}^{-1}[T(\mathbf{u})], \quad (5)$$

where $*$ is a convolution.

The Fourier transform (FT) of HREM images

$$I(\mathbf{u}) = \delta(0) + 2\sigma T(\mathbf{u})\mathcal{F}[\varphi(\mathbf{r})], \quad (6)$$

i.e.

$$I(\mathbf{u}) = \delta(0) + 2\sigma T(\mathbf{u})F(\mathbf{u}), \quad (7)$$

where $F(\mathbf{u})$ is the Fourier transform of the projected potential. In expression (7), $\delta(0)$ corresponds to the unscattered electrons which contribute to the image as a background.

$$I(\mathbf{u}) = 2\sigma T(\mathbf{u})F(\mathbf{u}) \quad (\text{for } \mathbf{u} \neq 0), \quad (8)$$

$$F(\mathbf{u}) = I(\mathbf{u})/2\sigma T(\mathbf{u}) \quad (\text{for } T(\mathbf{u}) \neq 0), \quad (9)$$

i.e. the FT of the image is proportional to the CTF and the FT of the projected potential.

For an ideal lens, i.e. one for which $T(\mathbf{u}) = -1$ for all values of \mathbf{u} .

$$F(\mathbf{u}) = -I(\mathbf{u})/2\sigma = \exp[i\pi]I(\mathbf{u})/2\sigma, \quad (10)$$

$$\varphi(\mathbf{r}) = \mathcal{F}^{-1}[F(\mathbf{u})] = -I(\mathbf{r})/2\sigma, \quad (11)$$

the image intensity is proportional to the negative of the projected potential, i.e. black features in HREM positives (low intensity) correspond to atoms (high potential). Thus the amplitudes of the FT of the HREM image ($I(\mathbf{u})$) are proportional to the FT of the projected potential ($F(\mathbf{u})$), while all the phases of the FT of the HREM image are shifted by 180° from those of the FT of the projected potential.

A typical contrast transfer function for a non-optimum defocus is shown in Fig. 1. Different Fourier components of the projected potential are transferred

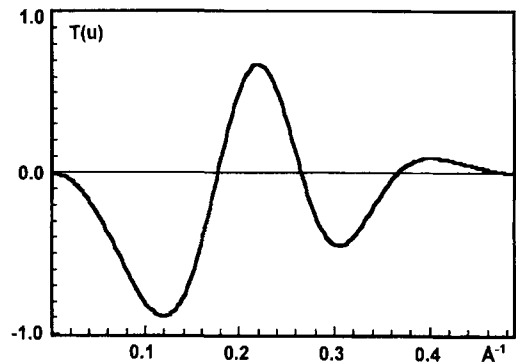


Fig. 1. A contrast transfer function $T(u)$ of a JEOL 200CX microscope at 200 kV. $C_s = 1.2$ mm, $\epsilon = -1400$ Å, focal deviation $\Delta = 150$ Å and beam divergence $\alpha = 0.037^\circ$ were used for calculating the CTF. The Fourier components of the projected potential with u in the ranges of $T(u) > 0$ give a phase contrast proportional to the projected potential, while those u in the ranges of $T(u) < 0$ give reversed phase contrast.

by the CTF into the HREM image in different ways, depending on the resolution range in which the Fourier component lies. Fourier components in the range $T(\mathbf{u}) > 0$ will be transferred to give rise to a contrast proportional to the projected potential. In the range where $T(\mathbf{u}) < 0$, all Fourier components will suffer a phase change of 180° , i.e. the contrast is reversed. An image taken at such a defocus is formed by a complicated mixture of Fourier components; some give correct contrast and some give reversed contrast.

Furthermore, the amplitudes of the Fourier components are attenuated by the CTF, i.e. by $|T(\mathbf{u})|$. The Fourier components with $T(\mathbf{u}) = 0$ will not be transferred by the lens. The areas where $T(\mathbf{u}) = 0$ are seen as dark rings in the FT of images. The defocus value can be determined from those \mathbf{u} values, if λ and C_s are known, using expressions (2) and (4).

For images free from astigmatism, the CTF will be circularly symmetrical, i.e. it has the same value for all Fourier components with the same resolution

(= $|\mathbf{u}|$ value). In astigmatic images the beam is focused asymmetrically by the objective lens, and so it can be considered as if the defocus values are different for different directions. The dark rings caused by the crossovers of the CTF will turn into ellipses (Fig. 2).

2.2. Determination of and correction for astigmatism and defocus

CRISP, a program system for crystallographic image processing has been developed in our group for solving unknown crystal structures from HREM images on a personal computer (PC). The first version of CRISP [9] ran directly under DOS, but now the program has been rewritten completely and it runs under Microsoft Windows[®]. HREM images in arbitrary sizes, digitised either by CCD camera or by other devices such as microdensitometers or slow scan CCD cameras can be processed by this system. A two-dimensional crystal structure determination of

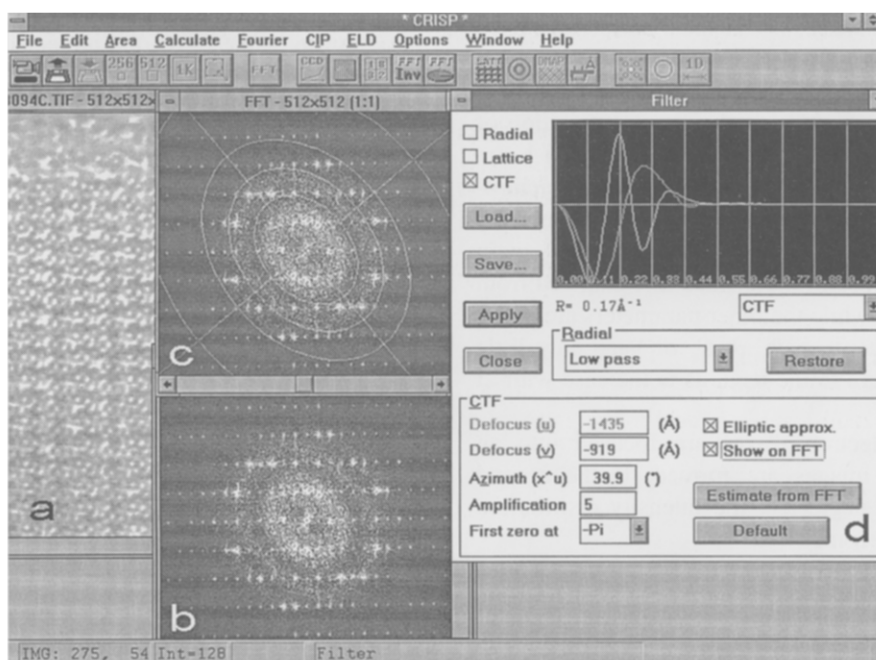


Fig. 2. An HREM image (a) is analyzed by CRISP. (b) An elliptical dark ring can be seen in the background noise of the Fourier transfer of the image. (c) A set of ellipses, available in the Filter tool, are fitted to the dark rings which correspond to the zero crossovers (nodes) of the CTF. (d) The defocus values along the minor and major axes are estimated from the innermost ellipse to be -1435 and -919 Å. The azimuth is 39.9° . The corresponding two CTF curves are shown in the Filter.

heavy atoms can be performed in minutes. The Windows version of CRISP contains several new features. One of these, an option for determining and correcting for defocus and astigmatism in the contrast transfer function, was used in the present investigation.

We used a thin crystal of $K_{8-x}Nb_{16-x}W_{12+x}O_{80}$ ($x \approx 1$) to study quantitatively how the CTF affects image contrast. This compound is isostructural to $Na_7Nb_{15}W_{13}O_{80}$ with unit cell dimensions $a = 22.0$, $b = 17.8$, $c = 3.9$ Å and space group $Pmab$ which has been solved and refined by single crystal X-ray diffraction [11]. HREM images in the [001] projection were taken at 200 kV under different experimental conditions in a JEOL 200CX microscope at a magnification of $690\,000\times$. The spherical aberration constant C_s of this microscope is 1.2 mm and the resolution limit at the optimum defocus is 2.5 Å. The focus spread Δ and the beam divergence α were assumed to be 150 Å and 0.037° , respectively. Heavy atom (Nb/W) positions of $K_{8-x}Nb_{16-x}W_{12+x}O_{80}$ were determined earlier by HREM and image processing from one of these images taken close to the optimum condition. Nb and W atoms are statistically distributed in this compound [12].

HREM images in positive paper prints were digitised by a CCD camera and transferred to a PC via a Shark frame grabber, using the CRISP input system. With this set-up low intensities $I(r)$ are black and come out as low numbers after digitisation. Each image with the size of 512×512 pixels corresponded to an area of 233×233 Å in the specimen. The amorphous regions at the edge of the crystal were included in the selected areas (Fig. 2a) since they facilitate in finding the contrast transfer function. Fourier transforms were calculated from the selected areas (Fig. 2b).

In the Fourier transforms (FT), the sharp diffraction spots come from the periodic features, while the diffuse background corresponds to the FT of the amorphous region. The elliptical dark ring in the Fourier transform of an image with astigmatism in Fig. 2b shows the first zero crossover of the CTF.

For astigmatic images a filter with a set of ellipses (Fig. 2c) can be created in CRISP to fit the shape of the CTF zero crossovers as seen in the Fourier transform (Fig. 2b). For each of the \mathbf{u} values along

the major and minor axes of the innermost ellipse, corresponding defocus value is calculated from expressions (2) and (4):

$$\chi(\mathbf{u}) = \pi\epsilon\lambda\mathbf{u}^2 + \frac{1}{2}\pi C_s\lambda^3\mathbf{u}^4 = n\pi \quad n = 0, \pm 1, \quad (12)$$

$$\epsilon = \frac{n}{\lambda\mathbf{u}^2} - \frac{1}{2}C_s\lambda^2\mathbf{u}^2 \quad \mathbf{u} \neq 0. \quad (13)$$

For images taken near the optimum defocus, the first zero crossover is at $n = 0$. For more underfocused images $n = -1$ while overfocused images have $n = +1$. These different cases can be distinguished from the positions of the second and third zero crossovers (if visible in the FT) or by comparing the background noise distribution. A similar scheme was presented by Krivanek [13].

From the defocus values ϵ_u and ϵ_v along the major and minor axes of the ellipse and the azimuth θ_0 (the \mathbf{u} -axis is θ_0 degrees anti-clockwise away from the positive horizontal x -axis), the defocus value along each direction in the FT is calculated. The defocus $\epsilon(\theta)$ along the direction θ degrees away from the x -axis in the FT, as suggested by Henderson et al. [6], is

$$\epsilon(\theta) = \epsilon_u \cos^2(\theta - \theta_0) + \epsilon_v \sin^2(\theta - \theta_0). \quad (14)$$

The corresponding contrast transfer function $T(\mathbf{u})$ along this direction is then calculated using the expression (2). Two CTF curves for the two extreme defocus values ϵ_u and ϵ_v are shown in Fig. 2d. It is worth mentioning that the two extreme defocus values in expression (14) do not need to have the same sign. If one is underfocus and the other is overfocus, the first zero crossover will form a hyperbolic curve instead of an ellipse.

Once the CTF has been determined as above, it can be corrected for, as suggested by Schiske [4] and applied by among others Unwin and Henderson [5]. When the CTF is applied, the complex $I(\mathbf{u})$ is corrected by multiplying each pixel by $-1/T(\mathbf{u})$ at that position in the FT. In order to avoid magnifying highly uncertain data near the nodes of the CTF, no pixels will be amplified more than a user-specified number N , for example 5. When $|1/T(\mathbf{u})| > N$ (Amplification in Fig. 2), $I(\mathbf{u})$ will only be magnified by N .

The above mentioned method compensating for

the CTF assumes that amplitudes at the CTF crossovers in the Fourier transform of the images are exact zero. However, the experimental $I(\mathbf{u})$'s at the crossovers are not exactly zero. This is due to the doubly scattered electrons transferred by the lens by $\cos \chi(\mathbf{u})$ [14]. At the zero crossovers of the CTF ($\sin \chi(\mathbf{u})$), the elastically and kinematically scattered electrons are not transferred by the objective lens. Thus the contribution by the inelastic scattering and double scattering becomes significant. When amplitudes at the zero crossovers are not zero, one should be cautious with the amplitude correction of the CTF. In our case we did not correct amplitudes for the CTF effects. Since phases are more important for solving structures, as long as phases are corrected, we can obtain the correct structure projection.

The effects of correcting amplitudes for the CTF are illustrated in Fig. 3, which is the Fourier transform of Fig. 2b after the CTF correction using the Filter tool. The defocus values are $\epsilon_u = -1435 \text{ \AA}$, $\epsilon_r = -919 \text{ \AA}$, the azimuth $\theta_0 = 39.9^\circ$ and $N = 10$. The white rings indicate the CTF crossovers, which are generated by the over-compensation of the CTF.

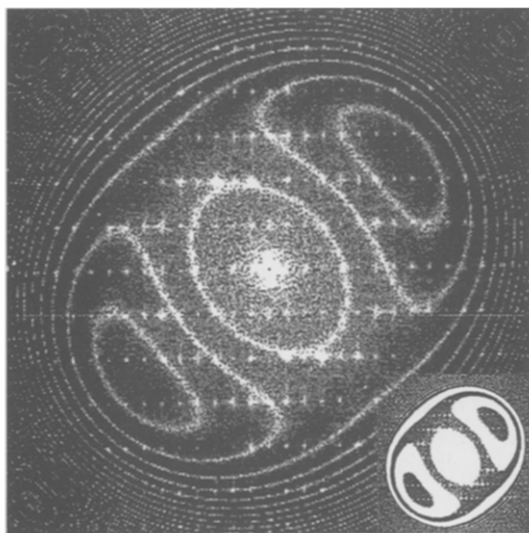


Fig. 3. Diffractogram of an image taken under non-optimum defocus and with astigmatism after the amplitudes have been corrected for the CTF. The defocus values $\epsilon_u = -1435 \text{ \AA}$, $\epsilon_r = -919 \text{ \AA}$ and the azimuth $\theta_0 = 39.9^\circ$ are used. The white rings outline the CTF crossovers. The inset shows the areas where $T(\mathbf{u}) > 0$ in black and $T(\mathbf{u}) < 0$ in white.

The effects on the phases of a CTF with astigmatism are demonstrated with the help of these white rings. One of the regions on either side of a white line has correct phases, the other region reversed phases.

2.3. Crystallographic image processing

The Fourier transform of periodic objects, such as HREM images of crystals, will have discrete diffraction spots, where $F(\mathbf{u})$ becomes $F(hk)$ which corresponds to the structure factor for electrons.

The principal procedures of crystallographic image processing of inorganic crystals were described earlier [9,12]. Several new functions have been added in the Windows version of CRISP, such as automatic lattice refinement, automatic symmetry determination and peak searching and refining in the final density map. In the Lattice Refinement procedure the positions of the diffraction spots are detected in the Fourier transform and the lattice is refined (Fig. 4). Amplitudes and phases are extracted at the lattice positions.

In the Origin Refinement step the crystal symmetry is found. All the possible 2D symmetries (the 17 plane groups) are tested automatically. If, as in this case, the two unit cell dimensions differ by more than 10%, the three-, four- and six-fold symmetries which all require that $a \equiv b$ will not be tested. Notice that the amplitudes cannot be used to differentiate between different symmetries since the crystallographic

$$R_{\text{sym}} = \frac{\sum_{h,k} ||F(hk0)| - |F(-hk0)||}{\sum_{h,k} |F(hk0)|} \quad (15)$$

(RA% in Fig. 4) is identical for seven different symmetries. This is so because they all have the same amplitude relationship $|F(hk0)| = |F(-hk0)|$.

However, the phases can be used for symmetry determination since the phase relations are different for different symmetries. Unlike amplitudes, phases are not absolute values, but relative to an origin. For all centro-symmetric projections ($p2$, pmm , pmg , pgg , ...) the phases are restricted to either 0° or 180° , if the origin is chosen at a center of symmetry. In higher symmetries than $p2$ additional conditions come in. For example, in pmm all symmetry-related

pairs of reflections ($hk0$) and $(-hk0)$ must have equal phases. In pmg the phase relation is different; symmetry-related reflections have different phases if h is odd (when the glide plane is perpendicular to the \underline{b} -axis which gives a translation of $\frac{1}{2}\underline{a}$ along the \underline{a} -axis). The phase relations for $p2$ and the orthorhombic symmetries can be summarized as:

$p2$: no relations,

$$pmm \text{ and } cmm: \quad \varphi(hk0) = \varphi(-hk0), \quad (16)$$

$$pmg: \quad \varphi(hk0) = \varphi(-hk0) + h \cdot 180^\circ, \quad (17)$$

$$pgg: \quad \varphi(hk0) = \varphi(-hk0) + (h+k) \cdot 180^\circ. \quad (18)$$

In $p2$ the phases of individual reflections are set to

0° if they are between -90° and 90° , otherwise they are set to 180° . In the higher symmetries the phases for a group of reflections have to be judged together. Sometimes the experimental phases are contradictory. If for example $\varphi(520) = 53^\circ$ but $\varphi(-520) = -29^\circ$ in a projection with pmg symmetry, then one of these reflections must have severely wrong phase, since the reflections must have different phases (expression (17)).

In CRISP the phases for a group of symmetry-related reflections are set such that the weighted total phase error is the smallest possible. For each symmetry, the program calculates the average phase residual for all reflections relative to the origin. In the origin refinement step, the origin is shifted in small steps throughout the entire unit cell and at every step

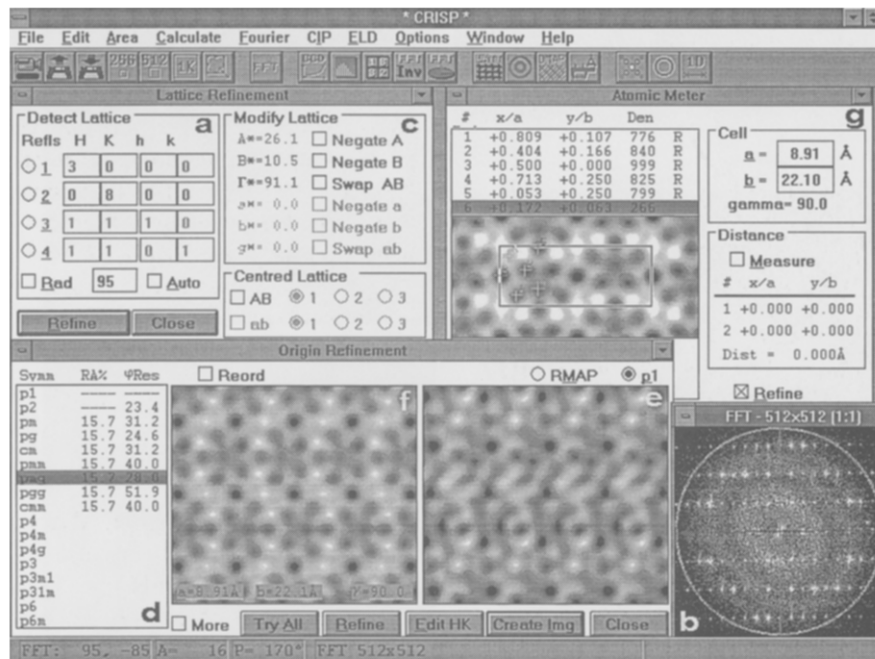


Fig. 4. Crystallographic image processing by CRISP. For the Lattice Refinement procedure, (a) Indices are given for two reflections (3 0) and (0 8), in the Fourier transform (b). The centers of all diffraction spots are found and the best lattice is fitted. (c) The lattice parameters are found to be 26.1 and 10.5 pixels along A^* and B^* respectively and the angle between them is 91.1° . We used only reflections inside 2.5 \AA resolution by placing a circle indicated in (b) with 95 pixels radius (Rad) as specified in (a). Amplitudes and phases are extracted from the refined lattice positions. In the Origin Refinement step (d), all 17 possible 2D symmetries are tested automatically and the corresponding figure of merit for amplitudes (RA%) and phases (φRes) are calculated. The symmetry pmg is chosen because it is the highest symmetry consistent with the image phases (phase residual 28.0°). Maps before (e) and after (f) imposing the symmetry pmg are displayed. Finally, using the Atomic Meter tool (g), fractional atomic coordinates and peak heights are obtained for each peak in the density map.

the average phase residual is calculated. The position where the phase residual is at its minimum is taken as the correct phase origin (Fig. 4).

If several reflections are symmetry-related and obey certain phase relations, their phases are determined by vector summation of all these reflections.

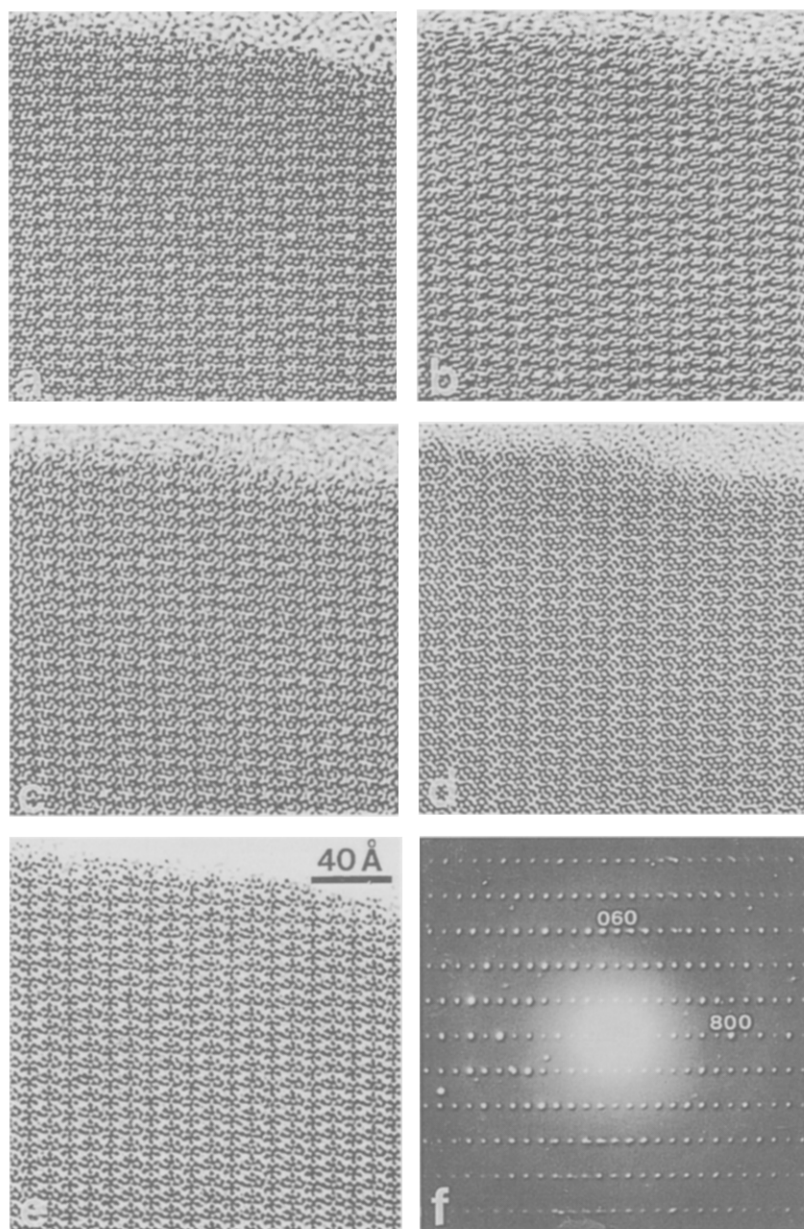


Fig. 5. (a–e) Five HREM images taken along the c axis from the same area of a crystal of $K_{8-x}Nb_{16-x}W_{12+x}O_{80}$, but taken under different optical conditions. Image features are very much different because the optical conditions are different. These five images are referred to as image a, b, c, d and e, respectively. (f) Electron diffraction pattern along the c -axis. Note that in this projection, the repeat along the b -axis is only half of the unit cell length (8.9 Å rather than 17.8 Å) because of the \bar{b} glide plane perpendicular to the c -axis. The repeating unit in this projection is 22.1×8.9 Å.

For centro-symmetric projections, they are further set to 0° or 180° .

The mean phase error (phase residual φ_{Res}) [12] is calculated as:

$$\varphi_{\text{Res}} = \frac{\sum_{h,k} w(hk0) |\varphi_{\text{obs}}(hk0) - \varphi_{\text{sym}}(hk0)|}{\sum_{h,k} w(hk0)}, \quad (19)$$

where $\sum_{h,k}$ is a sum for all h, k , $w(hk0)$ is a weighting factor (usually set to be equal to the amplitude of the reflection $(hk0)$), $\varphi_{\text{obs}}(hk0)$ and $\varphi_{\text{sym}}(hk0)$ are the observed and symmetrized phases, respectively.

The phase residual is a number which immediately tells how close the experimental phase data agrees with each symmetry. The highest symmetry which is still consistent with the experimental phases (i.e. giving a low phase residual φ_{Res}) is suggested as the correct symmetry of the crystal. In this case (Fig. 4d) the phase residuals were 40.0° for pmn , 28.0° for pmg and 51.9° for pgg . Thus pmn and pgg can be ruled out. But why do we conclude the symmetry is pmg rather than $p2$ or pg which have even lower phase residuals (23.4° and 24.6° , respectively)? The answer is that all higher symmetries always have lower sub-groups for which only part of the constraints need to be fulfilled. Thus a lower symmetry always gives similar or lower phase residual than the higher one. Whenever additional constraints on the phases can be added without a significant increase in the phase residual, this should be interpreted as indicating the higher symmetry. A quick inspection of Table 2, image c column should be enough to convince anyone that the phase values of pairs of reflection $(hk0)$ and $(-hk0)$ are not unrelated as in $p2$, but closely follow the much stricter rule given by the expression (17). Thus the projected symmetry of this crystal is pmg . This is also the projected symmetry of the isostructural compound $\text{Na}_7\text{Nb}_{15}\text{W}_{13}\text{O}_{80}$ (space group $Pmab$) [11].

The projected crystal symmetry is now imposed on both amplitudes and phases, and a density map is calculated by inverse Fourier transformation. This density map should correspond to the projected potential. Atomic coordinates and their peak heights can be obtained and refined by selecting the highest

peaks from the density map using the Atomic Meter tool (Fig. 4).

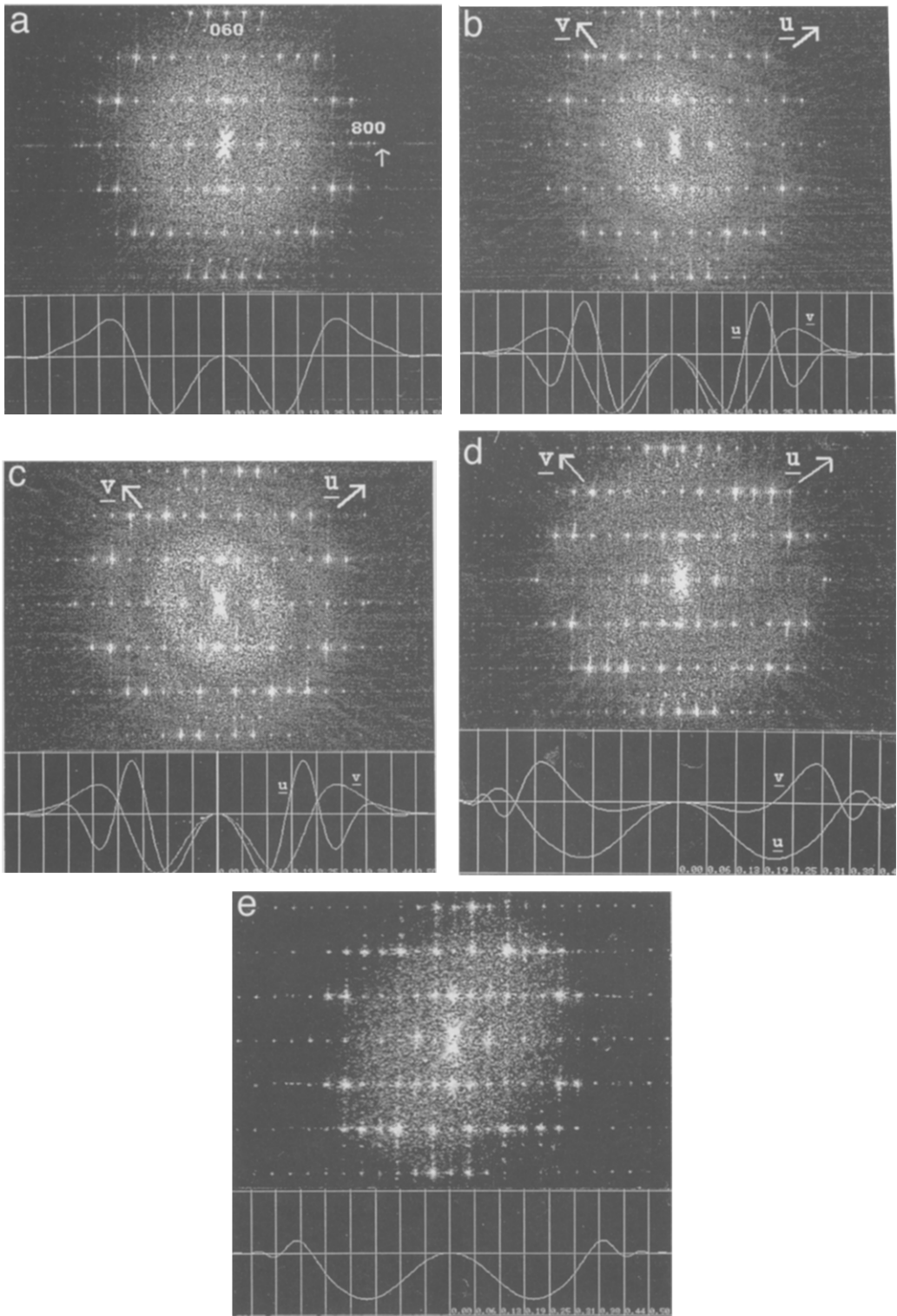
3. Results

Five HREM images of a uniformly thin crystal of $\text{K}_{8-x}\text{Nb}_{16-x}\text{W}_{12+x}\text{O}_{80}$ were processed by CRISP, applying this scheme for projected potential retrieval. All these images (Fig. 5) showed atomic resolution detail but they had very different contrast. From now on they will be called image a, b, c, d and e, respectively and will be described one by one. The images showed that the crystal was very thin and the weak-phase-object approximation should be valid. The electron diffraction pattern of the same projection (Fig. 5f) showed that reflections $(hk0)$ with $k = \text{odd}$ are absent, because of the glide plane perpendicular to the c -axis with the translation of $\frac{1}{2}b$ along the b -axis. Because of these absences, the repeating unit in this projection is $22.1 \times 8.9 \text{ \AA}$. The symmetry of the projected potential should be pmg , due to the glide plane perpendicular to the b -axis (with the translation along the a -axis) in space group $Pmab$.

3.1. Images with non-optimum defocus

Image a (Fig. 5a) was processed first. In the Fourier transform of the image (Fig. 6a), the white background noise was distributed cylindrically symmetrical, i.e. the astigmatism was negligible. Although there was no obvious dark ring present in the FT, one could see a sudden intensity decrease of the background at a resolution of about 4.5 \AA . If the image had been taken near the optimum defocus, a more gradual fading off of the background level should be seen at about 3 \AA resolution. Assuming this sudden intensity decrease was at a CTF crossover, the defocus value was estimated to be -988 \AA .

The density map obtained before the CTF correction is difficult to interpret in terms of the structure projection (Fig. 7a). After the phases in the image had been corrected for the CTF, using the CTF calculated from the defocus value -988 \AA (Fig. 6a), all metal atom positions could be recognised already from the density map before any symmetry was



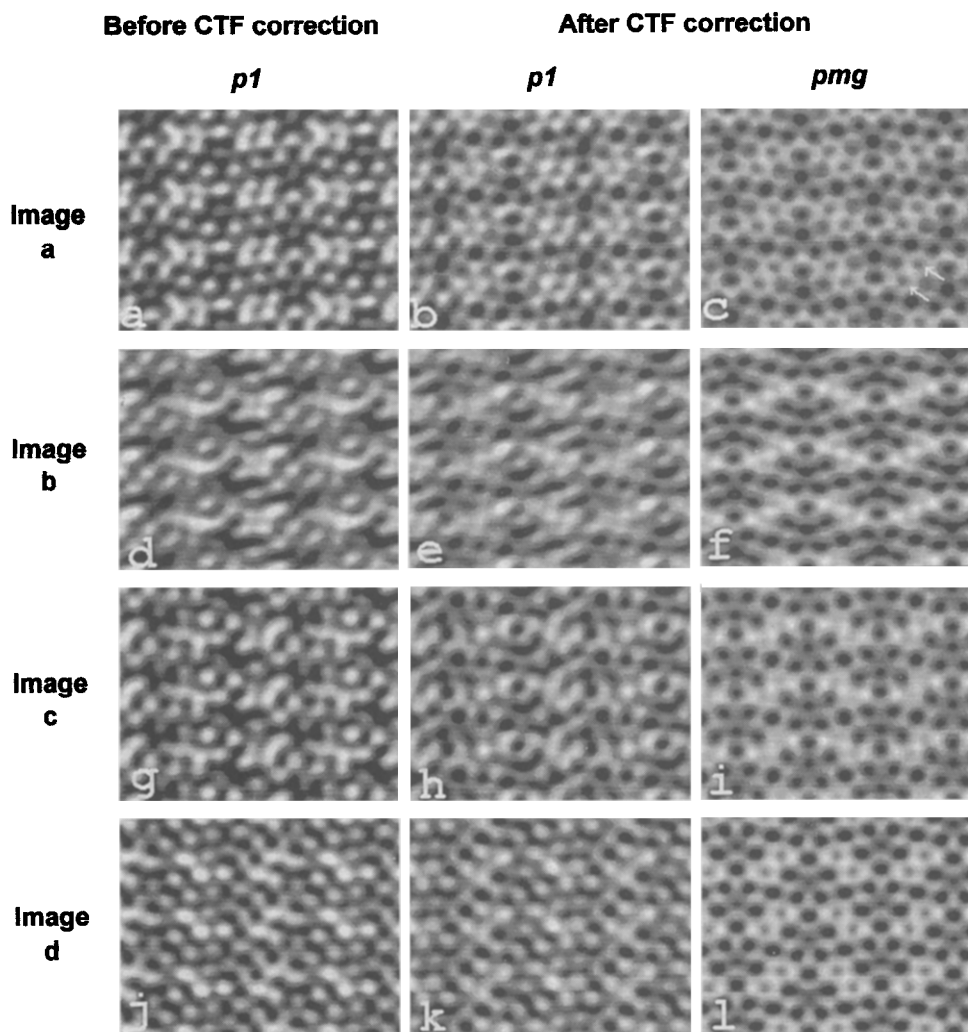


Fig. 7. Potential maps from four images taken under different optical conditions obtained by crystallographic image processing, to a resolution of 2.77 \AA : (a–c) from image a; (d–f) from image b; (g–i) from image c and (j–l) from image d in Fig. 4. The first column (a, d, g, j) are the $p1$ maps before CTF correction, i.e. only lattice averaging has been applied. None of them represents the projected potential. The second column (b, e, h, k) are the corresponding $p1$ maps after compensating for the astigmatism and defocus. Heavy atoms start to appear although they are not at exactly correct positions. The third column (c, f, i, l) are maps after imposing the crystallographic symmetry pmg into the CTF corrected maps. The large black peaks correspond to Nb/W positions and the smaller peaks, indicated by arrows in (c), are potassium atom positions.

Fig. 6. (a–e) The corresponding Fourier transforms of the HREM images (a–e) in Fig. 4. The scales of reciprocal vectors in the FT and the corresponding CTF under the FT are the same. The phases of reflections in the regions where the CTF lies above the zero line are shifted by 180° . (a) $\epsilon = -988 \text{ \AA}$ and no astigmatism. The first zero crossover of the CTF appears at the sudden decrease of the background noise in the FT. The arrow indicates the resolution of 2.5 \AA (0.40 \AA^{-1}). (b) $\epsilon_u = -1385 \text{ \AA}$ and $\epsilon_v = -895 \text{ \AA}$. (c) $\epsilon_u = -1435 \text{ \AA}$ and $\epsilon_v = -919 \text{ \AA}$. For both (b) and (c), within the resolution of 2.5 \AA , there are three zero crossovers along the u direction and only one along the v direction. (d) $\epsilon_u = -487 \text{ \AA}$ and $\epsilon_v = -160 \text{ \AA}$. The low resolution Fourier components along v are damped very much by the CTF and the corresponding background noise region is darker than that along u . (e) $\epsilon_u = \epsilon_v = -460 \text{ \AA}$.

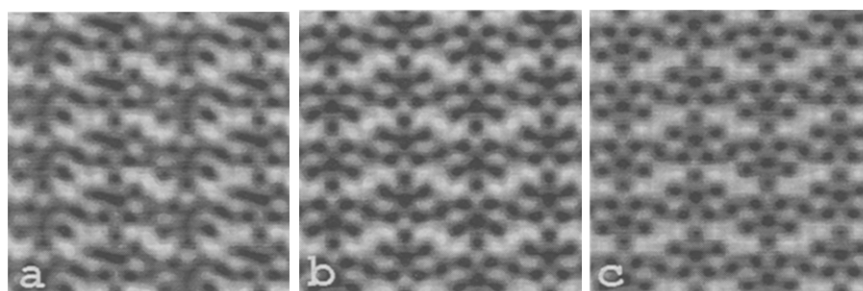


Fig. 8. Potential maps from image e in Fig. 4 taken near the optimum defocus obtained by crystallographic image processing, to a resolution of 2.77 Å: (a) *pI* map before CTF correction (b) *pmg* map before CTF correction (c) *pmg* map after CTF correction. The Nb/W atoms are better resolved in the map after CTF correction, but no potassium atoms can be seen.

imposed (*pI*) (Fig. 7b). However, the peak heights are very different. When the correct symmetry *pmg* was imposed, all metal atom positions were well

resolved and the heights of peaks became more equal (Fig. 7c). Note that the potassium atoms appear in this map, although they were not seen when the

Table 1

Amplitudes obtained from the Fourier transforms of HREM images a, b, c, d and e before the CTF correction and the corresponding R_{sym}

$h k l$	Image a	Image b	Image c	Image d	Image e	Combined $A(hkl)$	X-ray $F(hkl)$
2 0 0	5713	6792	6276	5841	7802	7802	2410
4 0 0	2426	1440	1899	318	1725	2426	2192
6 0 0	643	682	1524	248	676	1524	1106
8 0 0	947	431	851	1056	308	1056	4579
0 2 0	7758	10000	8464	5884	9313	10000	1655
1 2 0	4063	4787	3759	3198	4885	4885	1546
2 2 0	1873	1635	1708	2771	2878	2878	523
3 2 0	1584	1982	1968	2121	1463	1982	2741
4 2 0	274	584	592	847	454	847	293
5 2 0	1376	566	848	1109	805	1376	1415
6 2 0	4442	2554	5395	4107	3427	5395	7975
7 2 0	2107	891	1615	1895	1213	2107	6338
8 2 0	199	119	371	249	117	371	1084
0 4 0	2469	975	440	1227	694	2469	175
1 4 0	786	3636	3161	2274	4619	4619	3514
2 4 0	925	970	955	865	272	970	198
3 4 0	2764	4120	3291	4167	5823	5823	5941
4 4 0	1909	2332	2764	2735	1739	2764	2805
5 4 0	4035	2994	2804	5090	2202	5090	6584
6 4 0	883	415	871	1349	1133	1349	4267
7 4 0	193	77	313	234	169	313	68
0 6 0	2568	1215	875	3157	895	3157	4369
1 6 0	3390	3246	2315	3338	2214	3390	6050
2 6 0	2285	2691	1979	1924	845	2691	3952
3 6 0	373	578	614	368	182	614	1001
4 6 0	120	396	453	234	253	453	3711
R_{sym}	10%	20%	16%	23%	15%		

For each unique reflection ($h k 0$), the mean value of the symmetry-related reflections ($h k 0$) and ($-h k 0$) is given. The combined $A(hkl)$ is the highest amplitude from the five images. Amplitudes of X-ray structure factors $F(hkl)$ are listed. The five images were scaled together such that the sum of all amplitudes was the same for all images.

Table 2

Phases obtained from the Fourier transforms of HREM images a, b, c, d and e after CTF correction

<i>h k l</i>	Image a		Image b		Image c		Image d		Image e		Combined <i>pmg</i>	X-ray <i>pmg</i>
	<i>pl</i>	<i>pmg</i>										
2 0 0	0	0	24	0	21	0	0	0	11	0	0	180
4 0 0	-153	180	176	180	149	180	-128	180	176	180	180	180 [⊗]
6 0 0	25	0	-28	0	-41	0	36	0	2	0	0	180
8 0 0	169	180	97	180	111	180	42	0	-44	0	180*	0
0 2 0	167	180	177	180	176	180	180	180	178	180	180	0
-1 2 0	0	0	-23	0	-14	0	15	0	0	0	0	180
1 2 0	173	180	-179	180	174	180	-179	180	-174	180	180	0
-2 2 0	152	180	161	180	175	180	163	180	174	180	180	0
2 2 0	165	180	161	180	144	180	161	180	180	180	180	0
-3 2 0	165	180	179	0	174	0	-16	0	-2	0	0*	180
3 2 0	-10	0	-151	180	180	180	-157	180	-157	180	180*	0
-4 2 0	-83	180	158	180	173	180	-109	180	132	180	180	0
4 2 0	-173	180	-63	180	-82	180	114	180	149	180	180	0
-5 2 0	-16	0	-22	0	-29	0	-123	0	57	0	0	180
5 2 0	-153	180	40	180	53	180	-166	180	-173	180	180	0
-6 2 0	-173	180	-151	180	-127	180	-97	180	-158	180	180	0
6 2 0	-146	180	-162	180	-172	180	179	180	-144	180	180	0
-7 2 0	-179	180	-46	180	-42	180	-96	180	-169	180	180	0
7 2 0	35	0	-44	0	-32	0	0	0	100	0	0	180
-8 2 0	130	180	-81	0	-102	180	117	0	-99	0	0*	180
8 2 0	-154	180	-62	0	-128	180	-26	0	48	0	0*	180
0 4 0	-177	180	-179	180	94	180	125	180	46	0	180*	0
-1 4 0	-106	180	-174	180	-174	180	-175	180	163	180	180	0
1 4 0	57	0	7	0	-2	0	-22	0	-7	0	0	180
-2 4 0	149	180	171	180	176	180	-3	180	167	180	180	180 [⊗]
2 4 0	175	180	-179	180	109	180	-160	180	148	180	180	180 [⊗]
-3 4 0	161	180	175	180	180	180	174	180	180	180	180	0
3 4 0	-2	0	54	0	-51	0	16	0	15	0	0	180
-4 4 0	-170	180	-170	180	-159	180	-153	180	-168	180	180	0
4 4 0	-164	180	-84	180	-105	180	-131	180	-139	180	180	0
-5 4 0	0	0	16	0	58	0	44	0	11	0	0	180
5 4 0	-107	180	-82	180	-137	180	-86	180	-73	180	180	0
-6 4 0	-137	180	-2	180	46	180	-116	180	24	180	180	0
6 4 0	-140	180	126	180	-130	180	-129	180	133	180	180	0
-7 4 0	37	0	-26	180	129	0	-177	180	91	180	180*	0
7 4 0	-58	180	47	0	142	180	-114	0	21	0	0*	180
0 6 0	144	180	-164	180	122	180	135	180	155	180	180	0

Table 2 (continued)

Phases obtained from the Fourier transforms of HREM images a, b, c, d and e after CTF correction

<i>h k l</i>	Image a		Image b		Image c		Image d		Image e		Combined	X-ray
	<i>pl</i>	<i>pmg</i>	<i>pmg</i>	<i>pmg</i>								
2 0 0	0	0	24	0	21	0	0	0	11	0	0	180
-1 6 0	168	180	164	180	-166	180	144	180	160	180	180	0
1 6 0	-28	0	-12	0	-3	0	-35	0	-8	0	0	180
-2 6 0	180	180	180	180	-162	180	138	180	129	180	180	0
2 6 0	-163	180	-145	180	-154	180	156	180	-153	180	180	0
-3 6 0	26	0	21	0	28	0	-12	0	98	0	0	180
3 6 0	-148	180	-140	180	-150	180	20	180	165	180	180	0
-4 6 0	94	0	124	180	144	180	175	0	31	0	0 *	180
4 6 0	-81	0	-127	180	50	180	-38	0	35	0	0 *	180
Phase residual	16.3		21.5		28.9		24.9		15.5			

Columns *pl* and *pmg* contain phases before and after imposing symmetry, respectively. The combined phases deduced from all five images and phases of X-ray structure factors are listed. Reflections with uncertain phases are marked by *. Note that phases from HREM are opposite to those from X-ray, except for those marked by ☒.

Table 3

Atomic coordinates (*x/a* and *y/b*) and the corresponding peak heights (Den) for the metal atoms (Me = Nb/W) in $K_{8-x}Nb_{16-x}W_{12+x}O_{80}$ determined from different HREM images by image processing and in the isomorphous compound $Na_7Nb_{15}W_{13}O_{80}$ determined by X-ray diffraction.

Atom		Image a	Image b	Image c	Image d	Image e	Image combined	X-ray 2D	X-ray 3D
Me(1)	<i>x/a</i>	0.113	0.117	0.106	0.113	0.110	0.109	0.102	0.106
	<i>y/b</i>	0.403	0.403	0.405	0.407	0.408	0.412	0.408	0.414
	Den	599	855	807	879	918	828	999	999
Me(2)	<i>x/a</i>	0.164	0.168	0.170	0.162	0.162	0.165	0.165	0.162
	<i>y/b</i>	0.212	0.204	0.204	0.206	0.206	0.208	0.206	0.206
	Den	837	937	898	918	948	902	982	860
Me(3)	<i>x/a</i>	0.000	0.000	0.000	0.000	0.000	0.000	0.000	0.000
	<i>y/b</i>	0.250	0.250	0.250	0.250	0.250	0.250	0.250	0.250
	Den	968	999	999	999	944	999	874	653
Me(4)	<i>x/a</i>	0.250	0.250	0.250	0.250	0.250	0.250	0.250	0.250
	<i>y/b</i>	0.352	0.348	0.354	0.350	0.352	0.350	0.360	0.351
	Den	999	979	857	838	999	878	803	631
Me(5)	<i>x/a</i>	0.250	0.250	0.250	0.250	0.250	0.250	0.250	0.250
	<i>y/b</i>	0.030	0.028	0.025	0.040	0.033	0.033	0.039	0.034
	Den	795	821	845	904	831	849	830	748
K(6)	<i>x/a</i>	0.057	–	0.063	0.055	–	0.051	0.052	0.059
	<i>y/b</i>	0.072	–	0.086	0.072	–	0.082	0.078	0.086
	Den	388	–	278	305	–	277	536	183

Columns a, b, c, d and e show the coordinates from image a, b, c, d and e, respectively. The last three columns show coordinates in the map obtained from the combined HREM data (Fig. 9a) and from X-ray diffraction data (Fig. 9b) truncated to 2.77 Å in 2D (X-ray 2D) and from the full 3D X-ray data to better than 1 Å resolution (X-ray 3D).

structure was determined from the image taken near the optimum defocus [12] in Fig. 8a.

Phases after the CTF correction and amplitudes are listed in Tables 1 and 2, column a. The phase residual of this image for the symmetry *pmg* is 16.3° . The R_{sym} is 10%. The atomic coordinates are listed in Table 3.

3.2. Images with non-optimum defocus and astigmatism

The Fourier transforms of images b and c are similar (Fig. 6b and Fig. 6c). Both have a similar dark elliptical ring caused by astigmatic CTF crossovers. Image processing showed that the azimuths of astigmatism for both images were the same (39.9°) (Fig. 6b and Fig. 6c). The first crossovers along the \underline{u} direction appeared at 0.18 and 0.17 \AA^{-1} , respectively. The maximum and minimum defocus values were -895 and -1385 \AA for image b and -919 and -1435 \AA for image c. In the Fourier transform of the image c, a second dark band at about 0.26 \AA^{-1} could be found along the \underline{u} outside the first dark elliptical ring (Fig. 6c). This corresponds to the second crossover of a CTF with the defocus value -1435 \AA . The dark band did not continue to form a complete ellipse since the defocus value close to \underline{v} was decreasing towards -919 \AA where the second crossover comes at very high resolution ($> 0.40 \text{ \AA}^{-1}$) where the damping is severe. Thus it is difficult to see the second crossover near \underline{v} . This is shown more clearly in Fig. 3. In Fig. 6b, the second crossover along the \underline{u} direction is at even higher resolution (0.28 \AA^{-1}) where the amplitudes are very much damped, so it is not visible.

The *pl* density maps from the two images before the CTF correction were different (Fig. 7d and Fig. 7g). However, after CTF correction, the *pl* (Fig. 7e and Fig. 7h) and especially the *pmg* maps (Fig. 7f and Fig. 7i) were similar for the two images. All heavy atoms were clearly resolved in both maps. The corresponding amplitudes and phases are listed in Tables 1 and 2 and the coordinates are listed in Table 3. Before the CTF correction, the phase residual for the symmetry *pmg* were 27.0° and 37.3° . After CTF correction, they decreased to 21.5° and 28.0° , respectively. The decrease of the phase residuals after correcting for the CTF indicates that the

astigmatism which destroys the symmetry has been compensated.

In the Fourier transform of image d, there was no dark ellipse. Instead there was a dark band 0.20 \AA^{-1} away from the center along the \underline{v} (Fig. 6d). This corresponds to the defocus values -487 \AA and -160 \AA along the axes \underline{u} and \underline{v} respectively. The azimuth is 38.1° . Along the \underline{v} -axis, amplitudes for the low resolution data ($< 0.20 \text{ \AA}^{-1}$) were damped very much and the corresponding background noise region was much darker than along the \underline{u} -axis (Fig. 6d).

After the phases had been corrected for the CTF effects, the final density map showed all metal atoms including the potassium atoms (Fig. 7l). Amplitudes and phases are listed in Tables 1 and 2. The phase residual for the symmetry *pmg* was 31.6° before and 24.9° after CTF correction. The R_{sym} was 23%. Atomic coordinates are listed in Table 3.

3.3. Images taken near the optimum defocus

The image e (Fig. 5e) was previously considered to be taken near the optimum defocus [12]. The crystal was slightly tilted, this could be seen clearly from the thick part of the crystal (data not shown). The asymmetric distribution of amplitudes in the Fourier transform of the image (Fig. 6e) is mainly due to the crystal tilt [15]. The FT shows a continuous decrease of the background noise. Already the *pl* map before CTF correction and symmetrization showed the atomic arrangement (Fig. 8a). After the *pmg* symmetry was imposed, all heavy atom positions were well resolved (Fig. 8b). By comparing the phases of this image with those deduced from the previous four images, it was found that phases at very high resolution ($> 0.34 \text{ \AA}^{-1}$) disagreed. Yet, the map agreed well with the projected potential because the high resolution Fourier components outside 0.34 \AA^{-1} were very weak. The defocus value was now estimated to be -460 \AA . After the CTF correction was applied, the atoms were even better resolved in the potential map (Fig. 8c). The phase residual for the symmetry *pmg* was 15.5° . The R_{sym} was 15%. The final phases were compared with those deduced from the previous four images. Out of 26 unique reflections up to 2.5 \AA resolution only one phase deviated, that of the weak reflection (800).

3.4. A combined map

From the amplitudes and phases deduced from the above five images (Tables 1 and 2), one combined set of structure factors was constructed. For each reflection, the amplitude was chosen as the maximum amplitude of the five images, as suggested by Erickson and Klug [3]. Out of 26 unique reflections 20 had the same phase value in all five images after they were corrected for the CTF. These phase values were then considered to be correct. In the six cases of ambiguous phases, the phase was chosen as that obtained from most images. For two reflections ((320) and (040)) four images indicated one phase but one image differed. For four reflections ((800), (820), (740) and (460)) the phase was quite uncertain, since three images indicated one phase value and two images indicated the opposite phase. These four reflections are the reflections with d -values between 2.50–2.77 Å. Thus, the phases outside the resolution of 2.77 Å can be considered as random and the reliable information in the HREM images only extended to 2.77 Å resolution. In the final calculation of the density maps, only those reflections within the resolution of 2.77 Å were included. The inverse Fourier transform of this combined amplitude and phase set gave a further improved map (Fig. 9a). This averaged map was similar to a 2.77 Å resolution electron density map calculated from the X-ray structure factors [11] (Fig. 9b). The metal atom positions obtained from Fig. 9a and Fig. 9b are

listed in Table 3, in the column Image combined and X-ray 2D, respectively.

The metal atom coordinates of the isostructural compound $\text{Na}_7\text{Nb}_{15}\text{W}_{13}\text{O}_{80}$ determined by X-ray crystallography are listed in the column X-ray 3D, Table 3. The heavy metal atom coordinates derived from each of the HREM images (Table 3, column a–e) were in close agreement with those of $\text{Na}_7\text{Nb}_{15}\text{W}_{13}\text{O}_{80}$. Every one of the five images had an averaged error of heavy metal positions of less than 0.15 Å. Image e gave the smallest error (0.06 Å). The combined map gave an error of 0.06 Å. These errors in atomic positions are mainly due to the limited resolution of the data (2.77 Å) and to the fact that only data from one projection ($hk0$) was used. We obtained similar errors (0.12 Å) in atomic positions when we calculated an electron density map from X-ray diffraction data, limited to ($hk0$) and the same resolution as in the HREM images. The sodium atoms in $\text{Na}_7\text{Nb}_{15}\text{W}_{13}\text{O}_{80}$ are statistically distributed at two positions differing by ~ 0.5 Å in this projection. The potassium atom coordinates listed in Table 3 are for the center of these two positions. The potassium positions from HREM images deviated from the sodium positions in the X-ray structure by 0.23 Å.

In principle also the amplitudes may be corrected, by multiplying by $1/T(u)$. However, we found this not to be very successful; the density maps looked better before than after applying this correction. In the density maps shown here (Figs. 7 and 8) ampli-

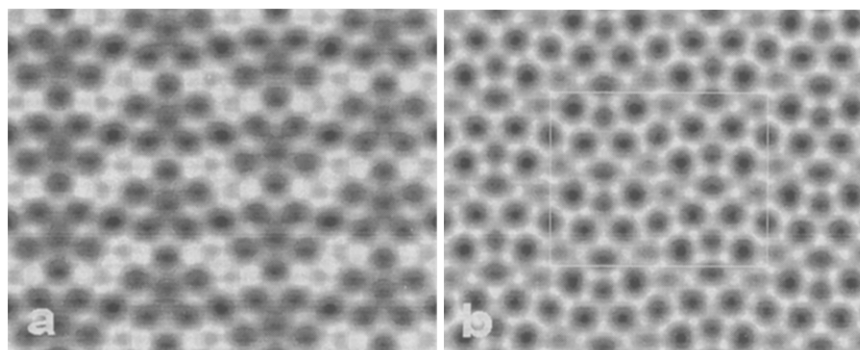


Fig. 9. (a) The potential map obtained by combining all five images a–e after CTF correction and symmetrization. (b) The density calculated from the structure model of $\text{Na}_7\text{Nb}_{15}\text{W}_{13}\text{O}_{80}$ determined by single crystal X-ray diffraction. The unit cell 22.0×17.8 Å is marked in (b). Data to 2.77 Å resolution was used.

tudes were not corrected for the CTF. Because of multiple scattering, not only the kinematical term, but also the term due to double scattering is enhanced [14].

With what precision must the defocus be known for the CTF reconstruction to be successful? We tested a wide range of defocus values for compensating the CTF for each of the images. We found that for image a, the reconstructed image showed the main structure features if the CTF was compensated for a defocus anywhere in the interval from -800 to -1100 Å, while $\epsilon = -988$ Å gave the best fit. For image e the corresponding defocus range was from -450 to -770 Å. For image b the ranges along the two extreme directions were $-1185 > \epsilon_u > -1535$ Å and $-870 > \epsilon_v > -980$ Å, while for image c the ranges were $-1355 > \epsilon_u > -1545$ Å and $-830 > \epsilon_v > -1170$ Å. For image d the ranges were $-70 > \epsilon_u > -380$ Å and $-467 > \epsilon_v > -800$ Å. In summary the ranges were typically about 300 Å. The accuracy of our method of defocus determination depends on the accuracy with which the crossovers can be estimated. In the present study we estimated that we could estimate the defocus to within ± 50 Å. This is well within the critical range ± 150 Å where the structure can be determined in CTF-corrected images.

4. Discussion

We have shown that the projected potential map can be retrieved from a single image taken under non-optimum conditions. The final maps from images taken at different defocus values are not completely identical, although they are very close, to the projected potential. The three main reasons for this are: Fourier components of the projected potential at the zero crossovers of the CTF are lost in the image; amplitudes affected by CTF are not corrected; and amplitudes obtained from HREM images are not very accurate. In order to obtain a better map, one can combine two or more images with different defocus values to fill up the missing regions in Fourier space, and use the maximum amplitudes from these images for substituting the image amplitudes, as we did to construct Fig. 9a. Of course the

best way is to combine a through-focus series of images.

Phases obtained from images after CTF correction are closely related to the X-ray structure factors. It can be seen from Table 2 that except for two out of 26 reflections, the EM phases are always opposite of the X-ray phases. This is because we have used the phases in the HREM images which are shifted by 180° from those of the projected potential in the crystal. Thus the phases of the X-ray structure factors are virtually identical to the phases of the potential as seen by electrons. We suggest that in the future the phases listed in electron crystallography investigations should be those of the potential. This would facilitate comparison between electron crystallography and X-ray crystallography results, and it would make it easier to incorporate the whole body of X-ray crystallographic techniques for solving and refining crystal structures into electron crystallography.

The reason why the phases differed between X-ray and EM for the two reflections may be that the atomic scattering factors for X-ray and electrons are different; or the occupancies of metal atoms in $K_{8-x}Nb_{16-x}W_{12+x}O_{80}$ may differ from those in $Na_7Nb_{15}W_{13}O_{80}$. One of the two reflections (240) is very weak which means its phase is relatively easy to change by any small factor. We intend to investigate this question by image simulation.

The close correspondence between phases from EM and X-rays further confirms that the WPO approximation is valid for a thin crystal even if it contains quite heavy atoms (Nb and W).

The phase errors at high resolution may be due to the errors in estimations of the CTF crossovers. In our study, we only used the first crossover in the Fourier transform of the images for estimating the experimental defocus ϵ . The CTF was then calculated from the defocus ϵ and the nominal value of C_s (1.2 mm). For large u the position of the CTF crossovers depend more on C_s than on ϵ in the expression (4). In order to estimate the high order zero crossover positions more accurately, one should use the calibrated C_s .

Although the amplitudes from the five images differ very much, the atomic positions obtained from the images are remarkably similar, with an average error of 0.15 Å from the positions determined by 3D

X-ray diffraction (Table 3). This means that good phases are more important than good amplitudes for determining atomic positions. However, errors in amplitudes make the relative peak heights different in different maps. This means that it is difficult to determine the relative occupancy of Nb/W in each position from our maps.

Even a slight crystal tilt, astigmatism or change in defocus will have a large effect on the amplitudes. Any combination of these may be the reason for the high R_{sym} -values. We intend to look into the effects of crystal tilt in more detail in a later paper.

One very significant result is that the potassium atoms could be revealed. In two images (a and d) the potassium atoms were well resolved and in two other images (b and c) they were hinted. Interestingly enough, in the image e, taken near the optimum defocus the potassium atoms were practically impossible to see. However, this image shows the most characteristic features of the structure and the Nb/W positions can be accurately determined.

The effect of a slight change in defocus is much larger for images taken away from the optimum defocus. As a consequence of this fact, the defocus values obtained by our method is less accurate near the optimum defocus ($\pm 100 \text{ \AA}$) than further away ($\pm 30 \text{ \AA}$). If the information limit in the images would have been at higher resolution, then an even more accurate defocus could be estimated, using the high order zero crossovers.

It is clear that in this case images taken under other defocus conditions contained more structure information than images taken at the optimum defocus. In general, the defocus to be selected for obtaining maximally the structure information depends on the structure projection of the crystal, which has not to be necessarily the optimum defocus of the microscope. However, the best way is to combine a through focus image series to obtain the complete structure information.

For images taken away from the optimum defocus, the high resolution structural information is only useful after image processing. In the near future, with the advent of electron microscopes equipped with field emission guns (FEG), this will become a very important issue. The wealth of high-resolution information from FEG instruments can only be made

use of if the images are properly computer processed.

This investigation has demonstrated that the projected potential of a thin metal oxide crystal can be reconstructed from images, which were distorted by defocus and astigmatism, by image processing. Here we have compensated for the effects of defocus and astigmatism. A study of simulated images of the silicate mineral orthopyroxene has shown that another factor which distorts HREM images, crystal tilt, can also be accurately determined and compensated for by image processing. This extended the range of interpretable images by about a factor of two in terms of crystal thickness or crystal tilt [15]. We are now investigating to what extent also the crystal thickness and crystal tilt of the $\text{K}_{8-x}\text{Nb}_{16-x}\text{W}_{12+x}\text{O}_{80}$ compound can be determined and corrected for using image processing. This will be done using both simulated and experimental HREM images.

5. Conclusions

Several HREM images of a $\text{K}_{8-x}\text{Nb}_{16-x}\text{W}_{12+x}\text{O}_{80}$ crystal taken under different defocus conditions with and without astigmatism were processed. The projected potential could be retrieved from any single HREM image, but the best results was obtained by combining information from several images taken at different defocus values. Using data to 2.77 \AA resolution, all heavy (Nb/W) atom positions could be found. Potassium atoms were not seen in any of the unprocessed images, but appeared after image processing in some of the images taken at non-optimum defocus values. Metal atom coordinates in projection were compared with those of the isostructural $\text{Na}_7\text{Nb}_{15}\text{W}_{13}\text{O}_{80}$ solved by single crystal X-ray diffraction. The coordinates were very similar, on average within 0.15 \AA .

Both astigmatism and defocus can be determined and then corrected for. In the present study, the defocus values are determined with an accuracy of about 50 \AA and the azimuth of astigmatism within 5° . The accuracy depends on the defocus and astigmatism values, as well as the microscope used. More coherent illumination and larger defocus give more

zero crossovers in the FT, thus more accurate defocus values can be obtained.

Phases from the Fourier transform of HREM images were the same as those of structure factors obtained from X-ray, except that all phase were shifted by 180° . However amplitudes differ very much from those obtained by single crystal X-ray diffraction. This difference may be due to crystal tilt or different relative scattering powers of Nb, W and oxygen atoms for electrons and for X-rays.

Acknowledgements

This project was supported by the Swedish Natural Science Research Council (NFR).

References

- [1] M.A. O'Keefe, *Acta Cryst. A* 29 (1973) 389.
- [2] F. Thon, *Z. Naturforsch.* 21a (1966) 476.
- [3] H.P. Erickson and A. Klug, *Phil. Trans. Roy. Soc. London B* 261 (1971) 105.
- [4] P. Schiske, in: *Electron Microscopy 1968, Rome, 1968*. Vol. 1, p. 145.
- [5] P.N.T. Unwin and R. Henderson, *J. Mol. Biol.* 94 (1975) 425.
- [6] R. Henderson, J.M. Baldwin, K.H. Downing, J. Lepault and F. Zemlin, *Ultramicroscopy* 19 (1986) 147.
- [7] D. Van Dyck and M. Op de Beeck, in: *Electron Microscopy 1990, Seattle, 1990*, p. 26.
- [8] W.O. Saxton, *Ultramicroscopy* 55 (1994) 171.
- [9] S. Hovmöller, *Ultramicroscopy* 41 (1992) 121.
- [10] M.A. O'Keefe, *Ultramicroscopy* 47 (1992) 282.
- [11] B.-O. Marinder and M. Sundberg, *Acta Cryst. C* 40 (1984) 1303.
- [12] S. Hovmöller, A. Sjögren, G. Farrants, M. Sundberg and B.-O. Marinder, *Nature* 311 (1984) 238.
- [13] O.L. Krivanek, *Optik* 45 (1976) 97.
- [14] X.D. Zou, *Electron Crystallography of Inorganic Structures – Theory and Practice*, *Chem. Commun.* 5, Stockholm University (1995) Doctoral Thesis.
- [15] X.D. Zou, E.A. Ferrow and S. Hovmöller, *Phys. Chem. Minerals* 22 (1995) 517.